Applied Catalysis A: General 506 (2015) 180–187

Contents lists available at ScienceDirect

Applied Catalysis A: General

journal homepage: www.elsevier.com/locate/apcata

AuFeAg hybrid nanoparticles as an efficient recyclable catalyst for the synthesis of α,β- and β,β-dichloroenones

Kanchan Mishra, Nagaraj Basavegowda, Yong Rok Lee*

School of Chemical Engineering, Yeungnam University, Gyeongsan 712-749, Republic of Korea

ARTICLE INFO

Article history:
Received 15 June 2015
Received in revised form 29 August 2015
Accepted 10 September 2015
Available online 12 September 2015

Keywords:
Hybrid nanoparticles
Astragalus membranaceus
Ferromagnetic
α,β- and β,β-dichloroenones

ABSTRACT

A facile and green pioneer approach for the synthesis of stable trimetallic AuFeAg hybrid nanoparticles is described. This synthetic method is green-chemistry compatible and totally free of additives. The particle shape and size, surface chemistry, crystallinity, elemental composition, thermal and magnetic properties were investigated. The catalytic performance of the synthesized nanoparticles is also described. The hybrid nanocatalyst exhibited strong catalytic activity for the synthesis of α,β- and β,β-dichloroenones, which are important synthetic intermediates in the preparation of natural products. The reason behind the catalytic performance of nano sized hybrid particles was attributed to their high specific surface area. In addition, the nanocatalyst was easy to separate from the reaction mixture using an external magnet and could be reused for five consecutive reactions without any significant loss of activity. Using the present method, the trimetallic hybrid combination can be designed for similar types of catalytic reactions.

© 2015 Elsevier B.V. All rights reserved.

1. Introduction

Hybrid nanoparticles with multifunctional materials accommodate a wide range of nanoscale domains into a single system that can exhibit enhanced properties, which are not available from their individual components. Heterogeneous hybrid nanoparticles with multiple domains in an epitaxial arrangement possess unique catalytic [1], magnetic [2], electronics [3], and optical properties [4]. Owing to its intrinsic robustness and potential feasibility, hybrid nanoparticles (NPs) have been developed and applied extensively in different technological fields. To synthesize these hybrid nanoparticles, one particle nucleates directly on the surface of another particle [5,6].

Many attempts have been made to synthesize multimetallic NPs because of their multiple advantages, including high selectivity and chemical/physical stability, compared to its monometallic components [7–10]. The properties of multimetallic NPs are affected entirely by their shape, similar to that of monometallic NPs. Moreover, the particle shape can determine the overall catalytic properties of NPs due to the different forms of exposed planes on their surfaces [11–13].

The authors' interest in developing a mild and efficient methodology to synthesize a variety of α, β-dihaloenones prompted the present study to search for more convenient and safer catalysts. To the best of the authors' knowledge, there are no reports on the phytosynthesis of AuFeAg hybrid nanoparticles and its catalytic application to synthesize α,β- and β,β-dichloroenones. Here the author's have used *Astragalus membranaceus* root extract for the synthesis of hybrid nanoparticles.

A. membranaceus (Fabaceae) is a perennial plant distributed widely in China and Korea and roots of it used mostly for immune stimulators and as a traditional medicine for anti-diabetic. The root of *A. membranaceus* contains several electron-rich molecules including saponins, polysaccharides, flavonoids, isoflavonoids, and sterols [14,15].

Molecules bearing α- and β-haloenones exist in nature and have potent biological activities [16–18]. They are important synthetic intermediates because a range of substituents can be installed at their α- and β-positions to synthesize biologically active natural products [19,20]. Because of their importance and utility, a range of synthetic methods have been developed for α- and β-haloenones [21,22]. The synthetic procedures for α-haloenones generally utilize halogenation–dehydrohalogenation [23], an addition–elimination [24], or halohydrin dehydration [25]. Recently, a number of synthetic approaches have been reported for β-haloenones, such as the Brønsted acid-promoted cyclization of 1-siloxy-1,5-diynes [26] and the halogen-induced 1,2-silyl migration reaction [27]. In addition, the 3-step synthetic route to α, β-dihaloenones from cyclohexane-1,3-dione has been reported [28]. Many methods for the synthesis of β-dichloroenones and α,

* Corresponding author. Fax: +82 53 810 4631.
E-mail address: yrlee@yu.ac.kr (Y.R. Lee).

http://dx.doi.org/10.1016/j.apcata.2015.09.014
0926-860X/© 2015 Elsevier B.V. All rights reserved.

β-dichloroenones have been well discussed, but these approaches have several shortcomings, such as the mixtures of products, low yields, low regioselectivity, and long reaction times.

Recently, to develop a protocol, we have reported on the synthesis of α,β- and β,β-dichloroenones by Ru(II)-catalyzed reactions of diazodicarbonyl compounds [29]. However, there is still a demand for novel and enhanced synthetic routes involving readily available and environmentally benign recyclable catalysts that efficiently provide a variety of α,β- and β,β-dichloroenones.This paper reports a facile and green approach for the synthesis of AuFeAg hybrid nanoparticles using *A. membranaceus* root extract as both the reductant and capping agent. The synthesized nanoparticles were used as catalysts for the synthesis of α,β- and β,β-dichloroenones from a diazodicarbonyl compound and oxalyl chloride.

2. Experimental

2.1. Materials and methods

Gold (III) chloride trihydrate ($HAuCl_4{\cdot}3H_2O$, 99.9%), iron (III) oxide (Fe_2O_3, 99%), and silver nitrate ($AgNO_3$, 99%) were obtained from Sigma-Aldrich. Oxalyl chloride and fluorobenzene were purchased from Tokyo Chemical Industries Co. Ltd. All chemicals were used as received. The air dried roots of *A. membranaceus* was obtained at a market in Yeongchon, South Korea. The *A. membranaceus* root extract was prepared using a previous method [30]. 6 g of the powdered roots was added to 300 mL of deionized Milli-Q water, boiled for 10 min and filtered.

2.2. Synthesis of AuFeAg hybrid nanoparticles

A volume of 10 mL of the root extract solution was added to 100 mL of an aqueous solution of 0.5 mmol Fe_2O_3 and sonicated for 1 h. After 1 h, the color of the solution changed to dark brown. To the solution, 5 mL of an aqueous solution of 2.0 mmol $AgNO_3$ was added and sonicated for 1 h. After 1 h, the color of the solution changed to dark blue, indicating the formation of FeAg nanoparticles. Again, 5 mL of an aqueous solution of 1.0 mmol $HAuCl_4$ was added and sonicated for 1 h at 60 °C. The color of the final solution changed to dark purple, indicating the formation of AuFeAg nanoparticles. The synthesized nanoparticles were isolated by centrifugation (10,000 rpm, 4 °C and 20 min) and purified twice by the addition of water, centrifuged and removed the supernatant.

2.3. UV–visible analysis of total phenolic acid present in A. membranaceus

The total phenolic acid present in *A. membranaceus* extract was determined by Folin–Ciocalteu's calorimetric method [31]. 1.5 mL of diluted Folin–Ciocalteu's reagent (2/20) was added in 1.0 mL of root extract, and allowed to stand for 5 min at room temperature. Then 1.5 mL of 7% sodium carbonate (w/v) was added to the mixture to neutralize it and kept in the dark at room temperature for 60 min. The absorbance was taken at 760 nm against a reagent blank. The result was expressed in grams of gallic acid equivalent (GAE)/(100 g dried weight of root).

2.4. Characterization of AuFeAg hybrid nanoparticles

The surface plasmon resonance was monitored using an Optizen 3220 (Double beam) UV–vis spectrophotometer with a quartz cuvette and distilled water as a reference. The Fourier transform infrared (FT-IR) spectra were recorded on a JASCO FTIR spectrometer in transmittance mode over the range of 400 - 4000 cm^{-1} and the samples were prepared by adding ~2 mg of dry powder with 200 mg of KBr to produce pellets for both the extract and nanoparticles. X-ray diffraction (XRD) was performed using powdered samples on a PANalyticalX'PertPRO MPD (operating at 40 kV and 30 mA with Cu Kα as the X-ray source (λ = 1.5406 Å) over the 2θ angle range, 20–90°, and a scanning rate of 1.2°/min). The size of the nanoparticles was assigned by field emission transmission electron microscopy (FE-TEM, FEI Tecnai F20). The samples were prepared by placing a drop of the nanoparticle solutions on carbon-coated copper grids and allowing the solvent to evaporate in air at ambient temperature. The elemental make-up of the bimetallic nanoparticles was analyzed by high-angle annular dark-field scanning TEM energy-dispersive X-ray spectroscopy (HAADF-STEM-EDS) at 200 kV with a point resolution of 0.24 nm, a Cs and Cc of 1.2 mm each and focal length of 1.7 mm, using a Genesis liquid nitrogen cooled EDS detector with an ultrathin window. The magnetic susceptibility and magnetization were investigated with by quantum design vibrating sample magnetometry (VSM Lake Shore Cryotronics, Inc., Idea-VSM, model 662 with 735 VSM controller) at room temperature in an applied magnetic field sweeping from −10 kOe to 10 kOe. The thermal properties of the nanoparticles were analyzed by thermogravimetric analysis coupled with differential scanning calorimetry (DSC-TGA, SDT-Q600 V20.5 Build 15) and heated under N_2 atmosphere to 700 °C at a heating rate of 10 °C min^{-1}. Atomic force microscopy (AFM, XE-100) has been assigned for sample surface characterization. AFM images were processed at resolution x, y: 0.1 nm and z: 0.01 nm. The composition of the nanoparticles and the chemical state of each element were analyzed by x-ray photoelectron spectroscopy (XPS) using a Thermo scientific, K-Alpha system fitted with an Al Kα X-ray light source. The ion source energy was 100 V to 3 KeV for the survey. Zeta-potential measurements were performed using a Malvern Zetasizer. The sample was equilibrated for 2 min at 25 °C and repeated three times for consistent results.

2.5. Catalytic activity

The resulting AuFeAg hybrid nanoparticles were used as a catalyst for the synthesis of α,β- and β,β-dichloroenones by reactions of diazodicarbonyl compound and oxalyl chloride.

2.5.1. General procedure for the synthesis of α,β- and β,β-dichloroenones

AuFeAg-NPs (3.5 mg, 1.0 mol.%) were added to a solution of cyclic or acyclic diazodicarbonyl compound (1.0 mmol) and oxalyl chloride (1.5 mL) in PhF (5.0 mL) at room temperature. The reaction mixture was stirred at 50 °C for 3 h or at room temperature for 5 h until the reaction was completed, as indicated by TLC. The solvent was evaporated under reduced pressure to give the residue. The residue was purified by flash column chromatography on silica gel with n-hexane/EtOAc (20:1) to give the product.

2.5.2. General procedure for the large scale synthesis of α, β-dichloroenones

AuFeAg-NPs (35 mg, 10.0 mol.%) were added to a solution of diazodicarbonyl compound **1a** (10.0 mmol, 1.660 g) and oxalyl chloride (15 mL) in PhF (10.0 mL) at room temperature. The reaction mixture was stirred at 50 °C for 3 h until the reaction was completed, as indicated by TLC. The solvent was evaporated under reduced pressure to give the residue. The residue was purified by flash column chromatography on silica gel using n-hexane/EtOAc (20:1) to give the product **2a** (1.785 g, 93%).

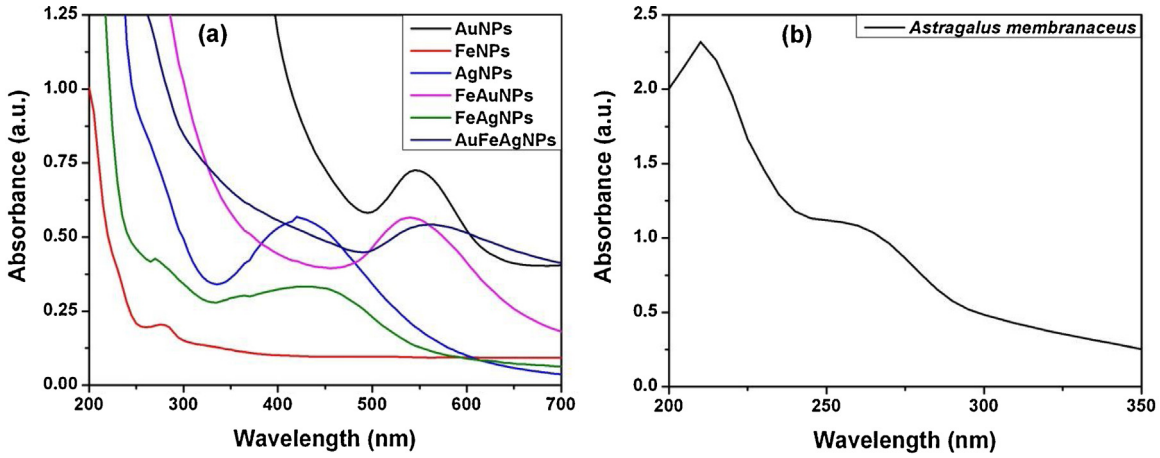

Fig. 1. UV–vis spectra of (a) AuNPs, FeNPs, AgNPs, FeAuNPs, FeAgNPs and AuFeAg-NPs and (b) *Astragalus membranaceus* root extract.

3. Results and discussions

3.1. Characterization of AuFeAg-NPs

The UV–vis absorption spectra of the Au, Fe, Ag, and AuFeAg nanoparticles in aqueous solution are shown in Fig. 1a. The AuFeAg hybrid nanoparticles manifested imprecise surface plasmon resonance that was different from the Au and Ag nanoparticles. The optical property was determined solely by the Au and Ag constituents. In AuFeAg, the surface plasmon of Au was red shifted from 540 nm to 560 nm and broadened. The surface plasmon of Ag was damped probably by AuFe, giving rise to continuous absorption, indicating the presence of iron oxide. The presence of bioactive molecules, such as polyols in the root extract was confirmed from the peaks observed at approximately 250–300 nm (Fig. 1b).

The capping of the nanoparticles by the root extract was observed by FTIR. Fig. S1, Supporting information shows the FTIR spectra of the root extract and AuFeAg-NPs. A comparison of the spectral data of the root extract revealed a decrease in the intensity of the peaks at 1055 and 1427 cm^{-1} in AuFeAg-NPs, indicating the surface capping of nanoparticles with methylene C—H rocking at 1404 cm^{-1} and C—O stretching at 1049 cm^{-1}.The absorption peak at 538 cm^{-1} was assigned to the Fe—O bond vibration [32]. The other absorption peaks at 3424 cm^{-1} and 1637 cm^{-1} were attributed to O—H and C=C stretching vibrations, which was slightly moved from 3393 and 1641 cm^{-1}, respectively. These results show that the bioactive molecules present in the root extract governed the reduction of metal ions and capping of the nanoparticles.

The role of *A. membranaceus* for the formation of nanoparticles is depicted in Scheme 1. The extract of *A. membranaceus* root contains several electron-rich molecules including saponins, polysaccharides, flavonoids, isoflavonoids, and sterols [14,15]. The hydroxyl and carbonyl groups of these compounds can reduce the metal salts to their nanoparticles via metal complexation and electron transfer. Thus, the metal salts of Au^{3+}, Ag^{+}, and Fe^{3+} were reduced to Au(0), Ag(0), and Fe^{2+}/Fe^{3+} nanoparticles, respectively, which were confirmed by the XPS analysis.

The powder XRD patterns of AuFeAg showed well resolved peaks (Fig. 2). The XRD peaks at 27.6, 32.0, 46.0, 54.5 and 57.3 2θ were indexed to the (2 2 0), (3 1 1), (4 0 0), (4 2 2), and (5 1 1) crystalline planes, respectively, corresponding to the face centered cubic (fcc) arrangement of iron oxide. Similarly, the peaks at 38.0, 44.2, 64.4, and 77.5 2θ were assigned to the (1 1 1), (2 0 0), (2 2 0), and (3 1 1) planes, respectively, due to the fcc arrangement of Au

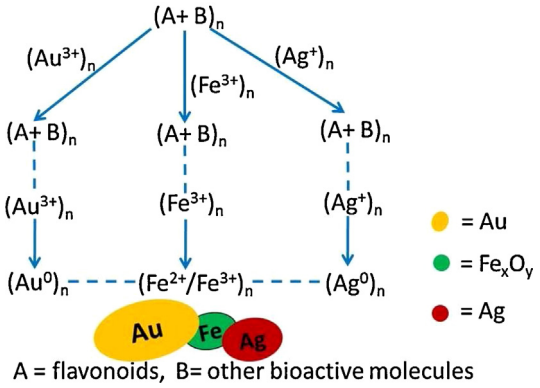

Scheme 1. Role of *Astragalus membranaceus* for the formation of AuFeAg-NPs.

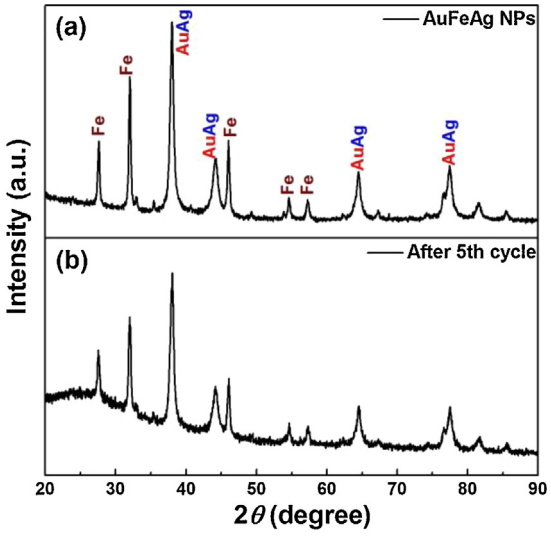

Fig. 2. XRD patterns of the AuFeAg-NPs (a) before reaction and (b) after five run.

(JCPDS no. 04-0784) and Ag (JCPDS no. 04-0783). This result confirms the crystalline nature of AuFeAg-NPs.

The elemental composition was examined by EDS analysis. TEM coupled with EDS showed typical optical absorption peaks at 0.8, 1.7, 2.2, 8.0, 9.8, and 11.4 keV (Fig. S2, Supporting information), which were assigned to the binding energies of iron, gold, and silver, further confirming the formation of AuFeAg-NPs.

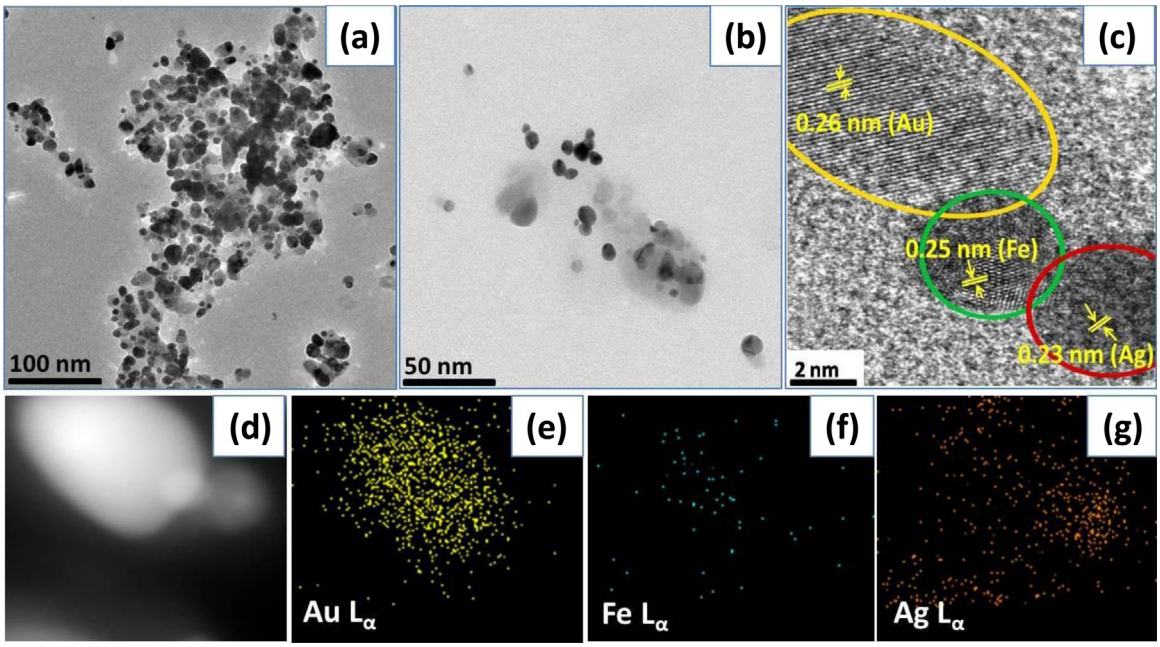

Fig. 3. TEM images of AuFeAg-NPs at magnifications of (a) 100 nm, (b) 50 nm, (c) HRTEM image with D-spacing. STEM image of (d) AuFeAg-NPs, along with the EDS elemental maps of (e) Au Lα shell, (f) Fe Lα shell, and (g) Ag Lα shell.

The size and morphology of the resulting nanoparticles were examined by TEM. Fig. 3a shows a TEM image of AuFeAg-NPs at 100 nm. Fig. 3b shows the dispersed ant-shaped nanoparticles at 50 nm scale bar. The high resolution TEM image in Fig. 3c shows the distinct crystalline lattice fringes of Au, Fe, and Ag. In addition, the interplane distance was 0.26 nm, corresponding to the (1 1 1) plane of the Au crystals. Similarly, the D-spacing was 0.25 nm, resembling the (311) plane of Fe [33], and the measured distance 0.23 nm, which is consistent with the (1 1 1) crystal plane of Ag [34]. HR-TEM revealed the ant-shaped AuFeAg nanoparticles with coherent interfaces; Ag (red circled) as the head, Fe (green circled) as neck and Au (yellow circled) as body shown in Fig. 3c. This epitaxial arrangement governed the stability of these interfaces [35,36]. In addition, high angle annular dark-field scanning transmission electron microscopy (STEM) (Fig. 3d), along with EDS elemental mapping confirmed the spatial arrangement of Au (Fig. 3e), Fe

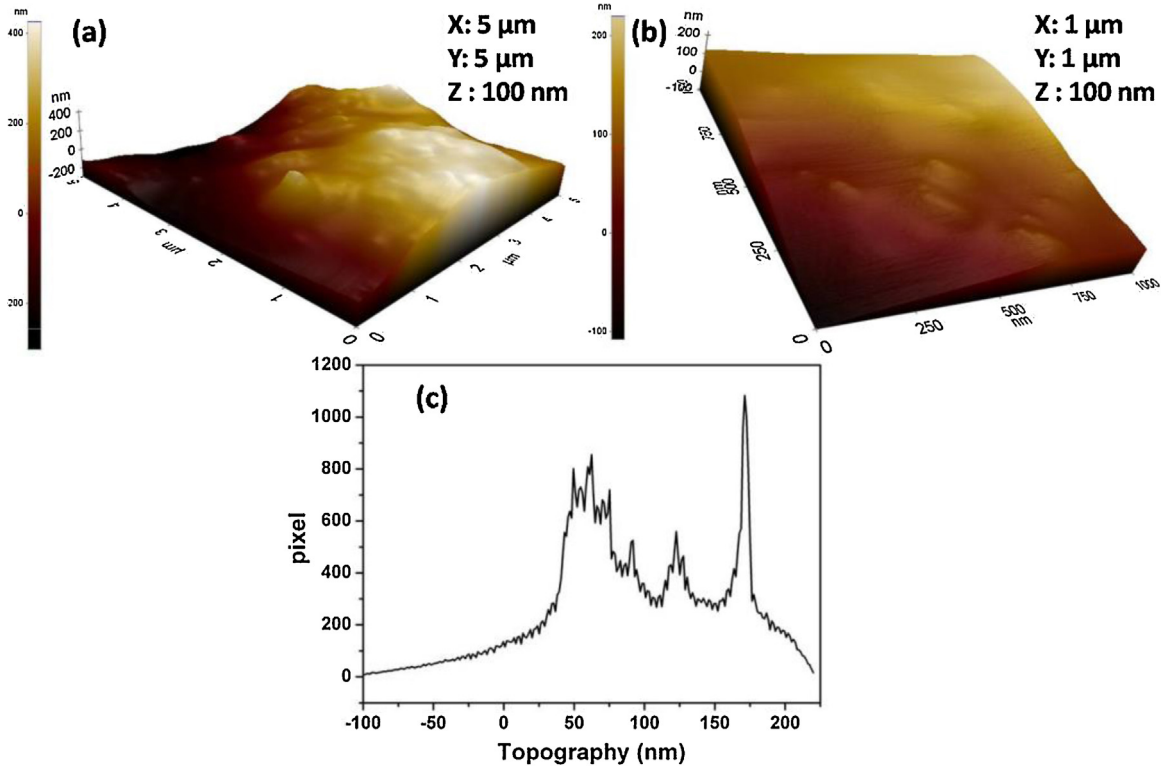

Fig. 4. AFM image of AuFeAg-NPs at (a) 5 μm^2, (b) higher magnification (1 μm^2) image, and (c) surface topography distribution of AuFeAg-NPs.

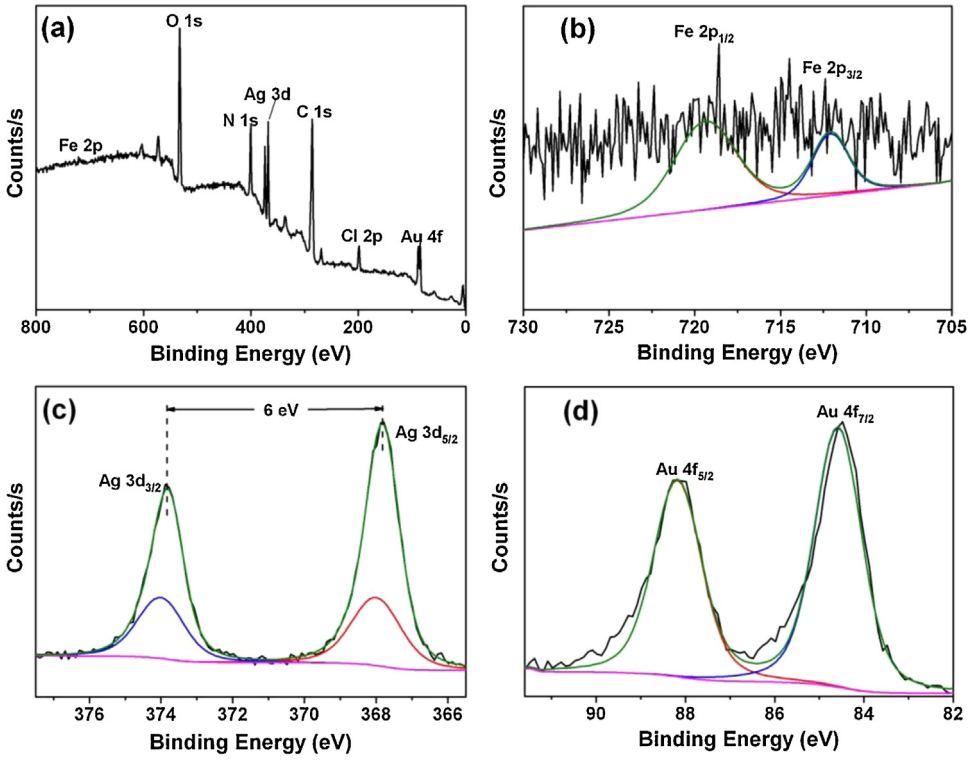

Fig. 5. XPS full scan survey of (a) AuFeAg-NPs, (b) Fe 3p-electrons of iron containing nanoparticles, (c) Ag 3d-electrons of silver containing nanoparticles, and (d) Au 4f-electrons of gold containing nanoparticles.

Table 1
Optimization of the reaction conditions for the synthesis of **2a**.[a–c]

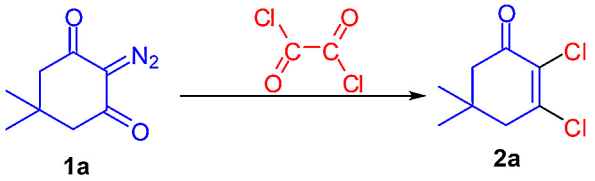

1a **2a**

Entry	Catalyst	Solvent	Time (h)	Conversion (%)	Yields (%)[b]
1	Au NPs	PhF	6	50	27
2	Fe NPs	PhF	9	12	5
3	Ag NPs	PhF	8	42	23
4	Fe-Au NPs	PhF	5	68	48
5	Fe-Ag NPs	PhF	8	60	42
6	AuFeAg NPs	PhF	3	99	92
7[c]	AuFeAg NPs	PhF	3	99	93
8	*Astragalus membranaceus* root extract	PhF	12	0	NR

NR- no reaction.
[a] Reaction conditions: diazo-dicarbonyls (1a, 1.0 mmol) and oxalyl chloride (1.5 mL) at 50 °C.
[b] Isolated yields.
[c] Diazo-dicarbonyls (1a, 10.0 mmol) and oxalyl chloride (15 mL) at 50 °C.

(Fig. 3f) and Ag (Fig. 3g), which further validated the linkage of Au (yellow) and Ag (red) by Fe (green) in the 3D core–shell nanostructures.

AFM was used to characterize the surface coverage of the AuFeAg hybrid nanoparticles. The AFM data were processed to 3-dimensional color map images. A higher or lower quality image is a great challenge due to the nature and position of the tip and other parameters, such as the scan rate, applied force and oscillation amplitude [37]. The AFM image at 5 μm^2 revealed the formation of a dense layer of nanoparticles on the silica plate with relatively low surface coverage (Fig. 4a). The higher magnification AFM image at 1 μm^2 also confirmed the relatively low coverage of the nanoparticles on the silica plate (Fig. 4b). The existence of nanosized Au, Fe and Ag particles in the as-synthesized trimetallic AuFeAg hybrid nanoparticles was confirmed in the three-dimensional AFM image. The results showed that the nanoparticles have a rough surface, and the particle distribution histogram showed that the AuFeAg nanoparticles have higher counts at 170 nm [38] (Fig. 4c).

XPS is an excellent technique for analyzing the oxidation state and surface chemistry of nanoparticles. The presence of gold, iron and silver in AuFeAg was manifested in the XPS measurements. Fig. 5a shows the XPS survey scan of AuFeAg nanoparticles. In the XP spectra of the Fe 2p electrons [39] (Fig. 5b), the 2p3/2 binding energy centered between 708.8 eV and 714.6 eV along with other strong peaks of 2p1/2 between 714.5 eV and 723.8 eV due to Fe^{2+}/Fe^{3+} were observed. The peaks observed including the shake-

Table 2
AuFeAg-NPs catalysed synthesis of a variety of α,β- and β,β- dichloroenones **2a–2k**[a–c].

entry	diazodicarbonyl compounds	products[d]	entry	diazodicarbonyl compounds	products[d]
1	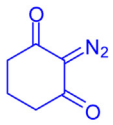 **1b**	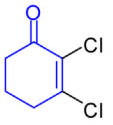 **2b**, 90% (99%)[b,c]	6	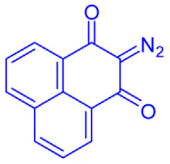 **1g**	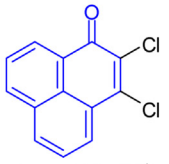 **2g**, 82%(95%)[b]
2	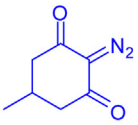 **1c**	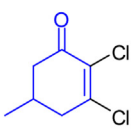 **2c**, 88%(97%)[b,c]	7	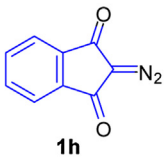 **1h**	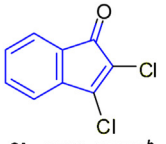 **2h**, 87% (92%)[b]
3	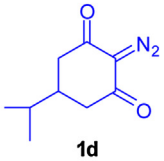 **1d**	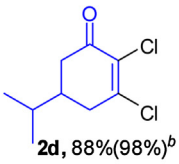 **2d**, 88%(98%)[b]	8	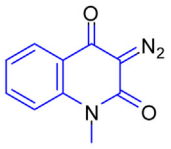 **1i**	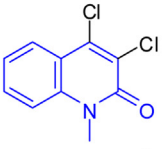 **2i**, 85% (90%)[b]
4	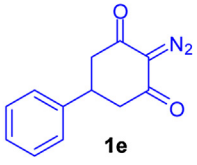 **1e**	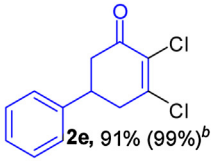 **2e**, 91% (99%)[b]	9	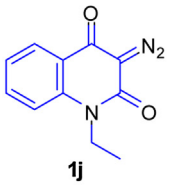 **1j**	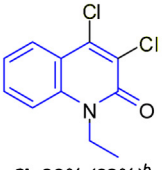 **2j**, 89% (92%)[b]
5	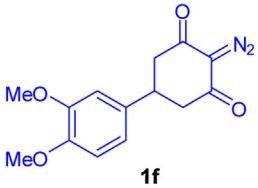 **1f**	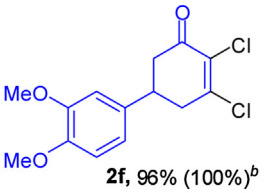 **2f**, 96% (100%)[b]	10	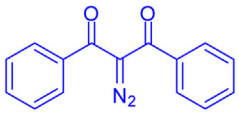 **1k**	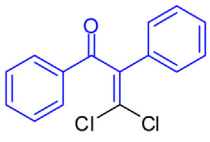 **2k**, 98% (100%)[b,c]

[a] Reaction conditions: diazo-dicarbonyls (1.0 mmol) and oxalyl chloride (1.5 mL) in presence of AuFeAg-NPs catalyst (1 mol %) in PhF (5.0 mL) at 50 °C for 3 h. [b] Number in parenthesis is conversion % of the starting material. [c] Reactions carried out at room temperature for 5 h. [d] Isolated yields.

up peaks are probably due to the different oxidation states of Fe (Fe^{3+} and Fe^{2+}). The XPS peaks of the Ag 3d electrons (Fig. 5c) appeared distinctly at 367.8 eV (3d5/2) and 373.8 eV (3d3/2) with a peak splitting of 6.0 eV, which confirms the metallic silver (Ag^0) [40]. An auger spectrum shows a small fraction of peaks at 374.0 and 368.0 eV, which may be due to the formation of a thin oxide layer over Ag NPs [41], while the immobilized AgNPs in hybrid form predominantly exist in their Ag (0) oxidation state. Similarly, the XPS spectra showed prominent peaks for the Au 4f electrons (Fig. 5d) at 84.5 eV and 88.2 eV binding energies, corresponding to 4f7/2 and 4f5/2, respectively. The doublet peaks along with the major peak at 84.5 eV (Au 4f7/2) are characteristic energy peaks of Au^0 [42]. This observation may be explained by the linkage of Au and Ag nanoparticles by Fe. Moreover, the XPS peaks at 532.0 and 585.0 eV were assigned to the O 1s and C 1s region respectively (Fig. S3, Supporting information). The atomic weight% of Au, Fe, and Ag assigned by XPS was found to be 29.65, 12.39, and 57.96 %, respectively (Table S1, Supporting information).

The thermal properties of AuFeAg-NPs were examined by Differential scanning calorimetry- Thermogravimetric analysis (DSC-TGA). TGA revealed the weight loss% during heating to 700 °C (Fig. 6a). The thermal decomposition of the nanoparticles took place in three steps. The initial weight loss around 100 °C (1.04 %) was attributed to the loss of adsorbed moisture and other volatile matter retained in the nanoparticles. The second stage occurred from 100 °C to 250 °C (6.88 %), which may be due to removal of the capping agents. The last step after 250 °C (17.59 %) was assigned to the loss of bioactive molecules present in *A. membranaceus* extract. The residual mass was found to be 74.49%, which confirmed the presence of gold, iron and silver in AuFeAg hybrid nanoparticles.

The DSC thermogram (Fig. 6b) revealed heat variations associated with an exothermic and endothermic reaction. The endothermic peaks observed at 197.57 °C and 308.43 °C, were

assigned to thermal decomposition of the bioactive molecules present in the root extract.

The total phenolic acid contents in the *A. membranaceus* root extract were found to be 1.5 ± 0.4 g of GAE/(100 g dried weight of root).

The hysteresis loops of AuFeAg-NPs provided by VSM analysis at 300 K (Fig. 7) revealed the nanoparticles to be ferromagnetic in nature with a saturation magnetization (Ms) of17.32 emu/g, so that the AuFeAg-NPs could be recovered from the reaction mixture by an external magnetic field. The coercivity (Hc) at 10 kOe and the remanent magnetization (Mr) were 0.18 kOe and 2.71 emu/g respectively.

The stability and the surface charge of the AuFeAg nanoparticles were performed using a zeta potentiometer [43]. The zeta potential distribution peak was found to be single peak (Fig. S4, Supporting information) and the average zeta potential value of the AuFeAg-NPs was -3.63 ± 0.62 mV (Table S2, Supporting information), which indicates the stability of the nanoparticles.

In order to check the reproducibility of the nanoparticles, three batches were prepared and their UV–visible spectra were observed. In their UV–visible spectra, the nanoparticles exhibited different surface plasmon resonance from Au as well as Ag nanoparticles. Red shift and broadening of the surface plasmon of Au in AuFeAg were observed, same to the initially prepared nanoparticles (Fig. S5a, Supporting information). Similarly, XRD patterns of the reproduced nanoparticles showed same patterns, confirming the formation of identical AuFeAg-NPs (Fig. S5b, Supporting information).

3.2. Catalytic activity

To synthesize a variety of α,β- and β,β-dichloroenone derivatives, reaction of cyclic diazodicarbonyl compounds (1.0 mmol) and oxalyl chloride (1.5 mL) were stirred in the presence of 1 mol.% of AuFeAg-NPs (3.5 mg) in PhF (5 mL) at 50 °C or room temperature. Treatment of the cyclic diazodicarbonyl compound **1a** with oxalyl chloride provided the product **2a** in 92% yield (entry 6, Table 1). Compound **2a** was determined by an analysis of its spectral data and by a direct comparison with the reported data (data presented in Supporting information) [29]. Importantly, when we tried the reaction of **1a** using AuFeAg-NPs in 10 mmol scale, the desired product **2a** was formed in 93% yield (entry 7, Table 1).

To examine the efficiency of hybrid AuFeAg-NPs, additional reactions of diazodicarbonyl compound **1a** with oxalyl chloride were performed in presence of the monometallic Au, Fe, and Ag nanoparticles and bimetallic FeAu and FeAg nanoparticles. Reactions using Au, Fe, and Ag nanoparticles afforded the desired product **2a** in 27, 5, and 23% yield, respectively. With bimetallic FeAu and FeAg nanoparticles, the yield was increased to 48 and 42%, respectively. Reaction in the presence of *A. membranaceus* extract without using any nanoparticles did not provide the desired product. Importantly, the use of hybrid AuFeAg-NPs provided the product in best yield (92%), compared to its mono- or bimetallic nanoparticles (Table 1).

To expand the scope of this reaction using hybrid AuFeAg-NPs, further reactions were next carried out (Table 2). For example, reactions of diazo dicarbonyl compounds **1b–f** with oxalyl chloride afforded **2b–f** in the range of 88-96% yield (entries 1–5, Table 2). With other diazo compounds **1g–j**, the desired products **2g–j** were isolated in 82-89% yield (entries 6-9, Table 2). In contrast with cyclic compounds, interestingly, reaction of acyclic diazodicarbonyl afforded the unexpected product. For example, treatment of 2-diazo-1,3-diphenylpropane-1,3-dione (**1k**) with oxalyl chloride in presence of AuFeAg-NPs (1 mol%) at room temperature for 5 h gave β, β -dichloroenone **2k** in 98% yield. The structure of **2k** was confirmed by comparison with spectral data of reported same compound [29]. The hybrid AuFeAg-NPs catalyzed reactions provided

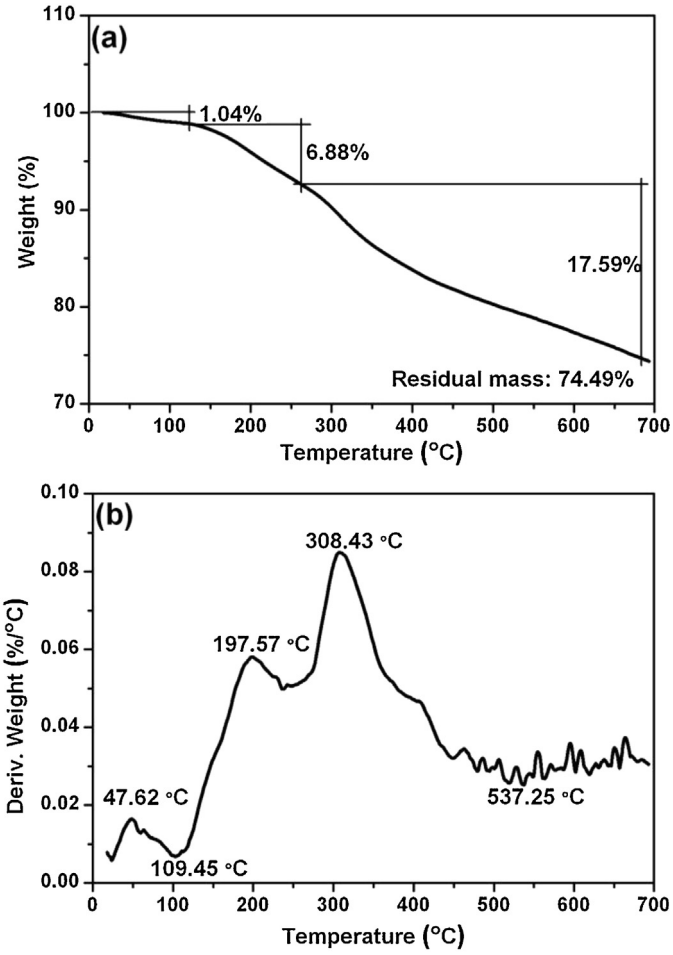

Fig. 6. (a) Thermogravimetric analysis trace of AuFeAg-NPs, and (b) Differential scanning calorimetry of AuFeAg-NPs.

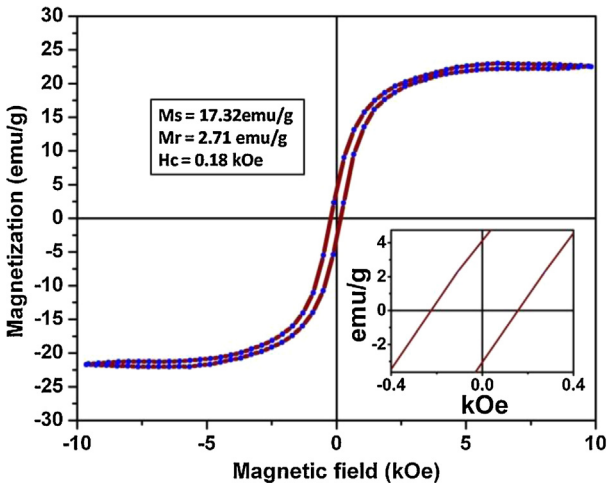

Fig. 7. Hysteresis loops of AuFeAg-NPs at 300 K and inset showing Mr and Hc.

a rapid synthetic route to α, β- and β, β -dichloroenones **2a–k** in excellent yields (Table 2).

The proposed mechanism for the formation of **2a** is described in Scheme 2. The displacement of nitrogen in **1a** by AuFeAg-NPs affords the metal carbenoid **3**. The chlorine atom of oxalyl chloride attacks the electrophilic carbenoid **3** to give the intermediate **4**, which undergoes intramolecular nucleophilic addition of oxygen atom to the carbonyl group of oxalyl chloride moiety followed by

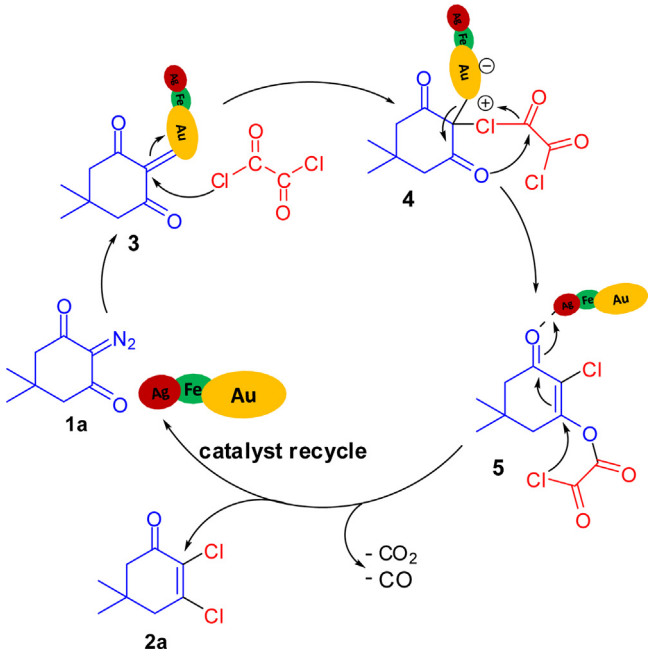

Scheme 2. Proposed mechanism for the formation of **2a**.

cleavage of the C—Cl bond to furnish the intermediate **5**. Finally, intramolecular nucleophilic addition of the chlorine atom to the enone moiety in **5** gives **2a** through decarboxylation and decarbonylation.

Furthermore, to investigate the performance of the AuFeAg-NPs catalytic systems for the synthesis of **2a**, reaction of **1a** was carried out for 10 h. In Fig. S6, Supporting information, the catalytic ability of AuFeAg-NPs exhibited good long-term behavior under the reaction condition applied. The conversion and yield did not vary throughout the time on stream from 3 h to 10 h.

Recyclability and stability are vital for estimating the performance of AuFeAg-NPs synthesized via a green approach. After the reaction, the catalyst was recovered by an external magnetic field due to the ferromagnetic nature of the nanoparticles. After separation, the catalyst was washed with CH_2Cl_2 and dried in a vacuum for 2 h. The recovered catalyst was then reused five times in subsequent reactions under identical conditions without any significant loss of catalytic activity, as shown in Fig. S7, Supporting information. The XPS peaks (Fig. S8, Supporting information) and XRD patterns (Fig. 2) of the AuFeAg-NPs were unchanged even after being recycled five times, which confirmed the retention of the catalytic activity without leaching of the hybrid nanoparticles.

4. Conclusions

Facile and stable trimetallic AuFeAg hybrid nanoparticles were synthesized by medicinally important *A. membranaceus* aqueous extract and characterized. The synthesized nanoparticles were used as convenient and green catalysts for the synthesis of α,β- and β,β-dichloroenone from diazodicarbonyl compounds and oxalyl chloride. After the reaction, the catalyst was recovered by an external magnetic field due to the ferromagnetic nature of the nanoparticles. The recovered unaltered catalyst was then reused five times in subsequent reactions under identical conditions without any significant loss of catalytic activity. These findings suggest that these magnetically retrievable nanoparticles can be used as a catalyst in a range of organic reactions.

Acknowledgements

This study was supported by the Nano Material Technology Development Program of the Korean National Research Foundation (NRF) funded by the Korean Ministry of Education, Science, and Technology (2012M3A7B4049675).

Appendix A. Supplementary data

Supplementary data associated with this article can be found, in the online version, at http://dx.doi.org/10.1016/j.apcata.2015.09.014.

References

[1] C. Wang, H. Daimon, S.H. Sun, Nano Lett. 9 (2009) 1493–1496.
[2] T. Teranishi, A. Wachi, M. Kanehara, T. Shoji, N. Sakuma, M. Nakaya, J. Am. Chem. Soc. 130 (2008) 4210–4211.
[3] R. Costi, G. Cohen, A. Salant, E. Rabani, U. Banin, Nano Lett. 9 (2009) 2031–2039.
[4] K.W. Kwon, M. Shim, J. Am. Chem. Soc. 127 (2005) 10269–10275.
[5] W. Shi, H. Zeng, Y. Sahoo, T.Y. Ohulchanskyy, Y. Ding, Z.L. Wang, M. Swihart, P.N. Prasad, Nano Lett. 6 (2006) 875–881.
[6] M. Casavola, R. Buonsanti, G. Caputo, P.D. Cozzoli, Eur. J. Inorg. Chem. 6 (2008) 837–854.
[7] N. Toshima, T. Yonezawa, New J. Chem. 22 (1998) 1179–1201.
[8] S.W. Kang, Y.W. Lee, M.J. Kim, J.W. Hong, S.W. Han, Chem. Asian J. 6 (2011) 909–913.
[9] L. Wang, Y. Nemoto, Y. Yamauchi, J. Am. Chem. Soc. 133 (2011) 9674–9677.
[10] Y. Xia, Y. Xiong, B. Lim, S.E. Skrabalak, Angew. Chem. Int. Ed. 48 (2009) 60–103.
[11] A.-X. Yin, X.-Q. Min, Y.-W. Zhang, C.-H. Yan, J. Am. Chem. Soc. 133 (2011) 3816–3819.
[12] R. Narayanan, M.A. El-Sayed, Nano Lett. 4 (2004) 1343–1348.
[13] J. Wu, A. Gross, H. Yang, Nano Lett. 11 (2011) 798–802.
[14] K. Agyemang, L. Han, E. Liu, Y. Zhang, T. Wang, X. Gao, Evid. Based Complement. Alternat. Med. 2013 (2013) 654643.
[15] Z. Zheng, D. Liu, C. Song, C. Cheng, Z. Hu, Chin. J. Biotechnol. 14 (1998) 93–97.
[16] T. Amagata, K. Minoura, A. Numata, J. Nat. Prod. 69 (2006) 1384–1388.
[17] G.M. Strunz, A.S. Court, J. Komlossy, M.A. Stillwell, Can. J. Chem. 47 (1969) 2087–2094.
[18] H.T. Dang, H.J. Lee, E.S. Yoo, J. Hong, B. Bao, J.S. Choi, J.H. Jung, Bioorg. Med. Chem. 16 (2008) 10228–10235.
[19] K. Li, A. Alexakis, Angew. Chem. Int. Ed. 45 (2006) 7600–7603.
[20] C.R. Johnson, M.P. Braun, J. Am. Chem. Soc. 115 (1993) 11014–11015.
[21] A.B. Smith III, S.J. Branca, N.N. Pilla, M.A. Guaciaro, J. Org. Chem. 47 (1982) 1855–1869.
[22] J.J. Janas, E.T. Asirvatham, E. McNelis, Tetrahedron Lett. 26 (1985) 1967–1968.
[23] C.J. Kowalski, A.E. Weber, K.W. Fields, J. Org. Chem. 47 (1982) 5088–5093.
[24] S. Kramer, S.D. Friis, Z. Xin, Y. Odabachian, T. Skrydstrup, Org. Lett. 13 (2011) 1750–1753.
[25] G. Righi, P. Bovicelli, A. Sperandio, Tetrahedron Lett. 40 (1999) 5889–5892.
[26] J. Sun, S.A. Kozmin, J. Am. Chem. Soc. 127 (2005) 13512–13513.
[27] N.T. Barczak, D.A. Rooke, Z.A. Menard, E.M. Ferreira, Angew. Chem. Int. Ed. 52 (2013) 7579–7582.
[28] H.W. Wanzlick, S. Mohrmann, Chem. Ber. 96 (1963) 2257–2258.
[29] K.B. SomaiMagar, Y.R. Lee, Adv. Synth. Catal. 356 (2014) 3422–3432.
[30] N. Basavegowda, K. Mishra, Y.R. Lee, New J. Chem. 39 (2015) 972–977.
[31] V.L. Singleton, J.A. Rossi, Am. J. Enol. Vitic. 16 (1965) 144–158.
[32] F.F. Bentley, L.D. Smithson, A.L. Rozek, Infrared Spectra and Characteristic Frequencies 700–300 cm^{-1}, Wiley (Interscience), NY, 1968.
[33] M.R. Buck, J.F. Bondi, R.E. Schaak, Nat. Chem. 4 (2012) 37–44.
[34] J.Q. Tian, S. Liu, Y.W. Zhang, H.Y. Li, L. Wang, Y.L. Luo, A.M. Asiri, A.O. Al-Youbi, X.P. Sun, Inorg. Chem. 51 (2012) 4742–4746.
[35] H. Yu, M. Chen, P.M. Rice, S.X. Wang, R.L. White, S. Sun, Nano Lett. 5 (2005) 379–382.
[36] C. Wang, H. Yin, S. Dai, S. Sun, Chem. Mater. 22 (2010) 3277–3282.
[37] M. Clemente-Leon, E. Coronado, A. Lopez-Munoz, D. Repetto, L. Catala, T. Mallah, Langmuir 28 (2012) 4525–4533.
[38] B. Loganathan, B. Karthikeyan, Colloid Surface A 436 (2013) 944–952.
[39] K. Mishra, N. Basavegowda, Y.R. Lee, Cat. Sci. Technol. 5 (2015) 2612–2621.
[40] S. Agnihotri, S. Mukherji, S. Mukherji, Nanoscale 5 (2013) 7328–7340.
[41] M. Schmidt, A. Masson, C. Brechignac, Phys. Rev. Lett. 91 (2003), 243401/1–243401/4.
[42] A. Pearson, A.P. O' Mullane, V. Bansal, S.K. Bhargava, Inorg. Chem. 50 (2011) 1705–1712.
[43] B. Loganathan, V.L. Chandraboss, S. Senthilvelan, B. Karthikeyan, Phys. Chem. Chem. Phys. 17 (2015) 21268–21277.